Efficiency Improvement of *LCC*-S Based IPT System by Detuning Design of the Secondary Side to Gain Unity Power Factor

Shufan Li, Fang Li, Rong Zhang, Lingbing Gong, Chengxuan Tao, and Lifang Wang, *Member, IEEE*

***Abstract*—To improve the power transfer efficiency (PTE) of the inductive power transfer (IPT) system based on *LCC*-S compensation network, a detuning design method of the secondary side is proposed in this article. First, time-domain analysis is used to model IPT system with a tuned and detuned secondary side, respectively. It was found that the reactive components brought by the rectifier can be compensated when the secondary side is detuned to a specific extent, thus gaining a unity power factor (UPF) in the secondary side. Then, design methods for the *LCC* network in the primary side both for fixed and variable load are proposed. Finally, simulations and experiments are conducted to verify the proposed modeling and designing method, with which the PTE can be improved in condition of coil misalignment and load variation, especially when the rectifier is in discontinuous conduction mode.**

***Index Terms*—Detuning design, efficiency, inductive power transfer (IPT), time-domain analysis (TDA).**

NOMENCLATURE

ω	Operating angular frequency of the system.
L_p, L_s, M	Self and mutual inductance of the coupling coils.
R_{LP}, R_{LS}	Parasitic resistance of the coupling coils.
L_f, C_f, C_p	Impedance compensating inductor and capacitors in *LCC* network.
α	Coefficient designed to realize the ZVS of the inverter.
C_s	Impedance compensating capacitor in the secondary side.
P_o	Output power of the system.
η	Power transfer efficiency (PTE).
I_p, I_s	Amplitude of current in coupling coils.
U_s	Amplitude of the induced voltage in the secondary side.
i_L	Current in L_s and C_s.
u_C	Voltage of C_s.
u_r	Input voltage of the rectifier.
U_{RL}	Voltage of the load.
V_{d_f}	Forward voltage of the diodes in the rectifier.
U_o	Input voltage of the rectifier in CCM.
I_o	Current in the load.
G	Ratio of U_o to U_s.
G_{c0}	Ratio of u_c (0) to U_s.
$i_{L\_1\mathrm{st}}$, $u_{r\_1\mathrm{st}}$	Fundamental components of i_L and u_r.
a_i, b_i, a_u, b_u	Coefficients of $i_{L\_1\mathrm{st}}$ and $u_{r\_1\mathrm{st}}$.
β	Ratio of R_L to ωL_s.
R_{rec}, X_{rec}	Real and imaginary parts of the equivalent input impedance of the rectifier.
R_{rec_β}, X_{rec_β}	Ratio of R_{rec} and X_{rec} to ωL_s.
θ	Leading angle of u_s to i_L.
φ	Discontinuous angle of i_L.
ω_0	Resonant angular frequency of L_s and C_s in detuned condition.
δ	Ratio of ω_0 to ω.
δ_{opt}	Optimum value of δ.
γ	Parameter derived from δ to simplify the deduction.
Z_{sec}	Input impedance of the secondary side.
X_{sec}	Imaginary part of Z_{sec}.
X_{sec_β}	Ratio of X_{sec} to ωL_s.
μ	Ratio of M to L_s.

Manuscript received 3 April 2023; revised 12 August 2023; accepted 19 September 2023. Date of publication 29 September 2023; date of current version 6 December 2023. This work was supported by the National Key R&D Program of China under Grant 2021YFB2501604. Recommended for publication by Associate Editor P. D. Mitcheson. *(Corresponding author: Shufan Li.)*

Shufan Li, Fang Li, Rong Zhang, Lingbing Gong, and Lifang Wang are with the Key Laboratory of Power Electronics and Electric Drives, Institute of Electrical Engineering, Chinese Academy of Sciences, Beijing 100190, China, and also with the University of Chinese Academy of Sciences, Beijing 100190, China (e-mail: lishufan@mail.iee.ac.cn; lifang@mail.iee.ac.cn; zhangrong@mail.iee.ac.cn; gonglingbing@mail.iee.ac.cn; wlf@mail.iee.ac.cn).

Chengxuan Tao is with the Key Laboratory of Power Electronics and Electric Drives, Institute of Electrical Engineering, Chinese Academy of Sciences, Beijing 100190, China, also with the University of Chinese Academy of Sciences, Beijing 100190, China, and also with the School of Mechanical Engineering, Beijing Institute of Technology, Beijing 100081, China (e-mail: taochengxuan@mail.iee.ac.cn).

Color versions of one or more figures in this article are available at https://doi.org/10.1109/TPEL.2023.3320656.

Digital Object Identifier 10.1109/TPEL.2023.3320656

I. INTRODUCTION

INDUCTIVE power transfer (IPT) technology [1], [2], [3] can transfer power wirelessly through magnetic coupling. In the past 20 years, this technology has witnessed its great development and wide utilization in electric vehicles [4], unmanned aerial vehicles [5], medical devices [6], portable electronics [7], and other industrial fields.

One of the mainstream applications of IPT system is the battery charger. A typical scenario is the charging of battery for the EVs. As shown in Fig. 1, the charging process of a battery in EVs usually contains constant current (CC) and constant

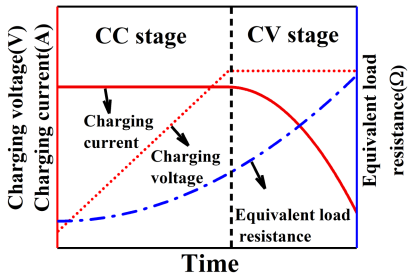

Fig. 1. Charging process of a battery of EVs.

voltage (CV) stage [8], [9]. The equivalent resistant load of the battery will increase with its voltage [10]. In CV stage, the value of the equivalent load will be so large that discontinuous conduction mode (DCM) of the rectifier may occur. Maintaining high power transfer efficiency (PTE) over the whole charging cycle is essential for an IPT system.

To improve the PTE, a variety of impedance compensation topologies are adopted, including four basic resonant networks, S-S, S-P, P-S, and P-P network [11], [12]. The S-S network is the most widely used with its simple structure and low cost [13]. One problem of the S-S network is the high sensitivity to the load variation [14], which will bring difficulties in controlling of the system. To solve this problem, optimum value of the load is elaborated in [15], [16], and [17], according to which the maximum efficiency tracking method is proposed. Another problem of S-S network is that the output power is inversely proportional to the mutual inductance of the coupling coils, overcurrent in the primary side may occur in misalignment occasions [18].

Higher order impedance matching networks are proposed in view of the high-sensitivity to parameters of S-S networks [14]. Among them, double-sided *LCC* network [19], [20], [21] and *LCC*-S [22], [23], [24] network are favored because primary coil behaves as a load and coupling factor independent CC source. The double-sided *LCC* network improves the designing freedom of the parameters, but it involves an inductor in the secondary side, which will occupy much more space than a single capacitor. Therefore, *LCC*-S network is favored in occasions where lightweight design is needed. To fit the charging requirement of a battery, a problem faced with the *LCC*-S network is the load variation. Different from the S-S network, with which the load can be tuned to the optimum one by control of the converters, the load of *LCC*-S based IPT system cannot be tuned in a wide range. The reason is that the induced voltage in the secondary side is constant, thus the duty ratio of the converter is determined by the output voltage (voltage of the battery in most conditions) which varies in a limited range. Therefore, the load of *LCC*-S based IPT system cannot be tuned to the optimum one in some occasions. The problem will be even more significant when the misalignment of coupling coils occurs.

Different parameter design methods [25], [26] and controlling strategies [24], [27], [28] have been studied to cope with the variation of the load as well as the coils misalignment. Besides, there have been studies about active or reconfigurable rectifiers [29], [30], improving the PTE for wide range of load by effective control of the converter. Switched controlled capacitor [31], [32], [33], [34] has been used to track the changes in coupling coils or load dynamically, and can also improve the tolerance of misalignment. In the above studies, the equivalent input impedance of the rectifier in the secondary side are usually considered as a resistive impedance according to first harmonic analysis (FHA) [35], which has been proved inaccurate especially in the DCM of the rectifier [36].

DCM usually occurs when the load of the IPT system deviates a lot from the nominal load [37]. To model the IPT system more accurately, numerical solutions of DCM are given in [37], which is simple but lacks universality. Time-domain analysis (TDA) are taken in [38] and [39], where nonlinear characteristics of the system caused by semiconductor MOSFETs or diodes are considered, and the TDA are used to depict both fundamental and harmonics of the waveforms and improve the modeling accuracy. In [36], both the primary and secondary side of an SS network based IPT system are modeled with TDA, which are proved superior to FHA. In one of the previous articles [40], TDA has been used to calculate the equivalent input impedance of the rectifier. Based on the TDA, it can be concluded that the equivalent input impedance of the rectifier is not resistive, leading to a nonunity power factor of the secondary side, which will bring reactive components to the system and lower the PTE.

To gain unity power factor (UPF) or nearly UPF, previous articles have been focused on designing of the compensation networks. In [41], an *LCLC* network is used to compensate for the reactive components caused by the nonlinearity of the rectifier. The harmonics in the secondary side are analyzed in [42] to model the system, and an inductor is used in series with the *CLC* network to compensate for the reactance resulting from rectifier operation in DCM mode, aiming to expand the range of CCM. Nearly UPF is realized in [43] by designing of a shunt inductor. The three works mentioned above have a common feature, which is the use of an inductor in the secondary side, which may increase the volume and costs of the system.

In summary, load variation of the IPT system can increase the reactive components, leading to low PTE, especially for light load condition when DCM of the rectifier occurs. By designing of the compensation networks, UPF or nearly UPF can be realized, but it usually involves higher complexity.

In this article, TDA is used to model the secondary side of an *LCC*-S based IPT system both in tuned and detuned conditions. In order to improve the PTE, reactive components in the secondary side are compensated by detuning design of the capacitor in series with the receiving coil. The parameters of the *LCC* network in the primary side have also been designed according to the fixed load and variable load, respectively. Compared with the previous article, the contributions of the article are as follows.

1) Depicting the nonlinear characteristics of the rectifier circuit in detuned conditions by accurate modeling of the secondary side with TDA.
2) Improving the PTE by detuning design of the impedance compensating capacitor in the secondary side.
3) Gaining UPF of the secondary side without adding any components.

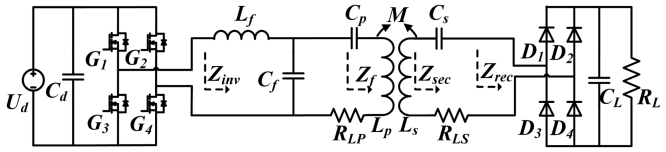

Fig. 2. *LCC*-S based IPT system.

II. IPT System Based on *LCC*-S Compensation Network

An IPT system based on *LCC*-S compensation network is shown in Fig. 2. L_P and L_S are self-inductance of primary and secondary coil, respectively, their mutual inductance is M, and R_{LP} and R_{LS} are their parasitic resistances. The full-bridge inverter contains four MOSFETs G_1–G_4, the output power of which will be tuned by the compensation network L_f–C_f–C_p. The impedance of the three arms of the compensation network should be equal, thus the values of L_f, C_f, and C_p are

$$\begin{cases} L_f = X_p/\omega \\ C_f = 1/X_p/\omega \\ C_p = 1/\omega/(\omega L_p - \alpha X_p) \end{cases} \tag{1}$$

where X_p is the impedance of the three arms, and α is used to realize the ZVS condition of the inverter. By changing α, the equivalent output impedance of the inverter is tuned, changing the turn-OFF current (I_{OFF}) of the MOSFETs without effect on the constant-current characteristic of *LCC* network [44]. The angular frequency $\omega = 2\pi f$, while f is the switching frequency of the inverter.

The amplitude of current in the primary-side coil is

$$I_p = \frac{4}{\pi X_p} U_d. \tag{2}$$

The capacitor C_s is used to form a resonant network with L_s, and it can be determined by

$$C_s = 1/\omega^2/L_s. \tag{3}$$

The rectifier contains four diodes D_1–D_4, and a capacitor C_L works as a voltage filter followed by the load R_L. With FHA method, the input impedance of the rectifier can be derived as

$$R_e = \frac{8}{\pi^2} R_L. \tag{4}$$

The amplitude of the induced voltage in the secondary side coil is

$$U_s = \omega M I_p. \tag{5}$$

The output power can be derived as

$$P_o = \frac{\omega^2 M^2 U_d^2}{X_p^2 R_L}. \tag{6}$$

The PTE is

$$\eta = \frac{P_o}{P_o + \frac{1}{2} I_p^2 R_{LP} + \frac{1}{2} I_s^2 R_{LS}} \tag{7}$$

where I_s is the amplitude of current in the secondary-side coil. The losses in the compensation networks are omitted, and there are two reasons for the neglection: 1) the main purpose of the article is to design the parameters of the compensation networks, and the parasitic resistances of the compensation networks are unknown before the designing, consequently the losses in the transceiving coils will be the main concern; and 2) in comparison of different designing methods, the losses in the compensation networks will be found nearly the same, which will be explained in detail in Section VI.

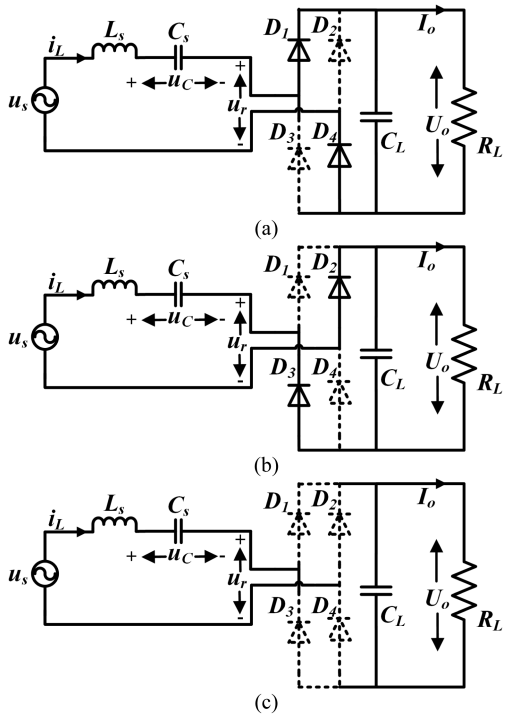

Fig. 3. Operating modes of the secondary side of the IPT system. (a) State 1. (b) State 2. (c) State 3.

III. Time-Domain Analysis of the IPT System With a Tuned Secondary Side

In a previous article, we have analyzed the *LCC*-S-based IPT system with a tuned secondary side in time domain [40]. In this article, we will analyze the detuned conditions (in the next chapter), and the results of analysis for tuned conditions will also be listed below to compare with the detuned ones. It should be noted that the deduction of tuned conditions will not be listed below since it can be referenced in [40].

In an IPT system with a tuned secondary side, the value of C_s is derived by (3). Based on the state of the four diodes of the rectifier, the operating modes of the secondary side of the IPT system can be divided into three states (states 1, 2, and 3 as shown in Fig. 3), which will be analyzed in detail below.

A. Continuous Conduction Mode (CCM)

Fig. 4 shows the waveforms of the secondary side, where u_s is the induced voltage of the secondary side, i_L is the current in L_s and C_s, u_C is the voltage of C_s, and u_r is the input voltage of the rectifier. To analyze the waveforms, we first assume a phase

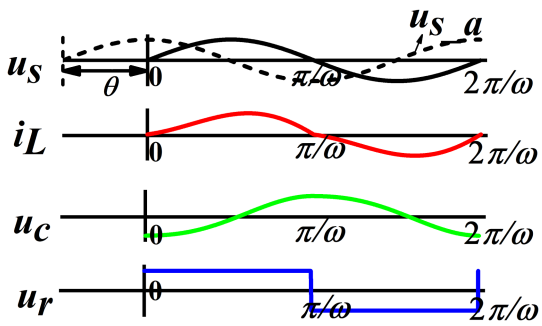

Fig. 4. Waveforms of the secondary side (CCM).

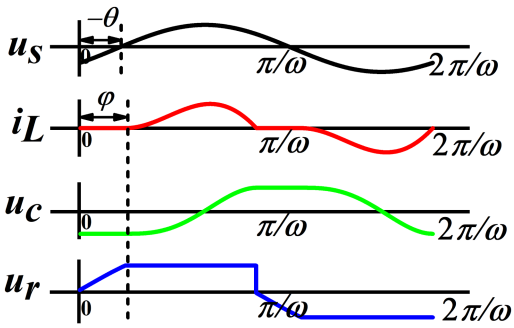

Fig. 5. Waveforms of the secondary side (DCM).

angle of u_s, i.e.,

$$u_{s\_a} = U_s \sin(\omega t + \theta). \tag{8}$$

According to [40], $\theta = 0$, and $i_L(t)$ can be derived as

$$i_L(t) = \begin{cases} \frac{U_s \sin(\omega t)}{\omega L_s}\left(\frac{1}{2}\omega t - \frac{\pi}{4} + \frac{\pi^2 \omega L_s}{8R_L}\right) & t \in [0,\ \pi/\omega] \\ \frac{U_s \sin(\omega t)}{\omega L_s}\left(\frac{1}{2}\omega t - \frac{3\pi}{4} + \frac{\pi^2 \omega L_s}{8R_L}\right) & t \in (\pi/\omega,\ 2\pi/\omega]. \end{cases} \tag{9}$$

As a square wave, $u_r(t)$ can be written as

$$u_r(t) = \begin{cases} U_o & t \in [0, \pi/\omega] \\ -U_o & t \in (\pi/\omega, 2\pi/\omega]. \end{cases} \tag{10}$$

The fundamental components of i_L and u_r can be written as

$$\begin{cases} i_{L\_1\mathrm{st}} = a_i \cos\omega t + b_i \sin\omega t \\ u_{r\_1\mathrm{st}} = a_u \cos\omega t + b_u \sin\omega t \end{cases} \tag{11}$$

where a_i, b_i, a_u, and b_u can be derived with

$$\begin{cases} a_i = \frac{\omega}{\pi}\int_0^{2\pi/\omega} i_L(t)\cos(\omega t)dt = -\frac{U_s}{4\omega L_s} \\ b_i = \frac{\omega}{\pi}\int_0^{2\pi/\omega} i_L(t)\sin(\omega t)dt = \frac{\pi^2 U_s}{8R_L} \\ a_u = \frac{\omega}{\pi}\int_0^{2\pi/\omega} u_r(t)\cos(\omega t)dt = 0 \\ b_u = \frac{\omega}{\pi}\int_0^{2\pi/\omega} u_r(t)\sin(\omega t)dt = U_s. \end{cases} \tag{12}$$

The real and imaginary part of the equivalent input impedance of the rectifier can be derived as

$$\begin{cases} R_{\mathrm{rec}} = \sqrt{\frac{a_u^2+b_u^2}{a_i^2+b_i^2}}\cos\left[\arctan\frac{b_u}{a_u} - \left(\pi - \arctan\frac{b_i}{a_i}\right)\right] \\ \quad = 8\pi^2 R_L / \left(\pi^4 + 4\beta^2\right) \\ X_{\mathrm{rec}} = \sqrt{\frac{a_u^2+b_u^2}{a_i^2+b_i^2}}\sin\left[\arctan\frac{b_u}{a_u} - \left(\pi - \arctan\frac{b_i}{a_i}\right)\right] \\ \quad = 16\beta R_L / \left(\pi^4 + 4\beta^2\right) \end{cases} \tag{13}$$

where

$$\beta = R_L/(\omega L_s). \tag{14}$$

The equations in (13) can be divided by ωL_s, i.e.,

$$\begin{cases} R_{\mathrm{rec}\_\beta} = 8\pi^2\beta/(\pi^4 + 4\beta^2) \\ X_{\mathrm{rec}\_\beta} = 16\beta^2/(\pi^4 + 4\beta^2) \end{cases} \tag{15}$$

where R_{rec_β} and X_{rec_β} are the ratio of R_{rec} and X_{rec} to ωL_s, separately.

B. Discontinuous Conduction Mode (DCM)

Fig. 5 shows the waveforms of u_s, i_L, u_C, and u_r in the DCM mode of the rectifier, and the discontinuous angle of i_L is φ. It should be noted that in this article, the use of C_L (shown in Fig. 2) as a filter is a necessary condition for DCM of the rectifier.

According to [40], i_L(t) can be derived as

$$i_L(t) = \begin{cases} 0 & t \in \left[0, \frac{\varphi}{\omega}\right] \\ \frac{U_s}{2\omega L_s}[(\omega t - \varphi)\sin(\omega t + \theta) \\ \qquad - \sin(\varphi + \theta)\sin(\omega t - \varphi)] & t \in \left(\frac{\varphi}{\omega}, \frac{\pi}{\omega}\right] \\ 0 & t \in \left(\frac{\pi}{\omega}, \frac{\varphi+\pi}{\omega}\right] \\ \frac{U_s}{2\omega L_s}[(\omega t - \varphi - \pi)\sin(\omega t + \theta) \\ \qquad - \sin(\varphi + \theta)\sin(\omega t - \varphi)] & t \in \left(\frac{\varphi+\pi}{\omega}, \frac{2\pi}{\omega}\right]. \end{cases} \tag{16}$$

$u_r(t)$ can be calculated by

$$u_r(t) = \begin{cases} U_s\left[\sin(\omega t + \theta) - \sin(\varphi + \theta) + G\right. & t \in [0, \varphi/\omega] \\ GU_s & t \in (\varphi/\omega, \pi/\omega] \\ U_s[\sin(\omega t + \theta) + \sin(\varphi + \theta) - G] & t \in (\pi/\omega, (\pi+\varphi)/\omega] \\ -GU_s & t \in ((\pi+\varphi)/\omega, 2\pi/\omega]. \end{cases} \tag{17}$$

The value of φ, θ, and G can be derived by solving

$$\begin{cases} \cos(2\varphi + \theta) + 2(\varphi - \pi)\sin\theta - \cos\theta = 0 \\ 2(\pi - \varphi)\cos\theta - 3\sin\theta - \sin(2\varphi + \theta) + 4\sin(\varphi + \theta) = 8G \\ \beta\left[2(\pi - \varphi)\cos\theta - 3\sin\theta - \sin(2\varphi + \theta) - 4\sin(\varphi + \theta)\right] = 4\pi G. \end{cases} \tag{18}$$

The fundamental components of i_L and u_r can also be written as (11), the same as CCM, but the values of a_i, b_i, a_u, and b_u are different, which can be derived as

$$\begin{cases} a_i = \frac{\omega}{\pi}\int_0^{2\pi/\omega} i_L(t)\cos(\omega t)\mathrm{d}t = \frac{U_s}{8\pi\omega L_s}\Gamma_1(\varphi, \theta) \\ b_i = \frac{\omega}{\pi}\int_0^{2\pi/\omega} i_L(t)\sin(\omega t)\mathrm{d}t = \frac{U_s}{4\pi\omega L_s}\Gamma_2(\varphi, \theta) \\ a_u = \frac{\omega}{\pi}\int_0^{2\pi/\omega} u_r(t)\cos(\omega t)\mathrm{d}t = U_s \sin\theta \\ b_u = \frac{\omega}{\pi}\int_0^{2\pi/\omega} u_r(t)\sin(\omega t)\mathrm{d}t = U_s \cos\theta \end{cases} \tag{19}$$

where

$$\begin{cases}\Gamma_1(\varphi,\theta) = (1+2\pi^2+2\varphi^2-4\pi\varphi)\sin\theta \\ \qquad\qquad +2(\varphi-\pi)\cos(2\varphi+\theta)-\sin(2\varphi+\theta) \\ \Gamma_2(\varphi,\theta) = (\pi^2+\varphi^2-2\pi\varphi-1)\cos\theta+\cos(2\varphi+\theta) \\ \qquad\qquad +(\varphi-\pi)\sin(2\varphi+\theta)+(\varphi-\pi)\sin\theta. \end{cases} \tag{20}$$

The equivalent input impedance of the rectifier is

$$\begin{cases} R_{\text{rec}} = \sqrt{\frac{a_u^2+b_u^2}{a_i^2+b_i^2}}\cos\left[\left(\pi - acr\tan\frac{b_u}{a_u}\right) - \left(\pi - acr\tan\frac{b_i}{a_i}\right)\right] \\ X_{\text{rec}} = \sqrt{\frac{a_u^2+b_u^2}{a_i^2+b_i^2}}\sin\left[\left(\pi - acr\tan\frac{b_u}{a_u}\right) - \left(\pi - acr\tan\frac{b_i}{a_i}\right)\right]. \end{cases} \tag{21}$$

Accordingly, $R_{\text{rec\_}\beta}$ and $X_{\text{rec\_}\beta}$ can be derived as

$$\begin{cases} R_{\text{rec\_}\beta} = \frac{8\pi[\sin\theta\Gamma_1(\varphi,\theta)+2\cos\theta\Gamma_2(\varphi,\theta)]}{\sqrt{\Gamma_1(\varphi,\theta)^2+4\Gamma_2(\varphi,\theta)^2}} \\ X_{\text{rec\_}\beta} = \frac{8\pi[-\cos\theta\Gamma_1(\varphi,\theta)+2\sin\theta\Gamma\Gamma_2(\varphi,\theta)]}{\sqrt{\Gamma_1(\varphi,\theta)^2+4\Gamma_2(\varphi,\theta)^2}}. \end{cases} \tag{22}$$

Assuming $\varphi = 0$, the critical condition of CCM and DCM can be derived as

$$\begin{cases}\theta = 0 \\ \beta = \frac{\pi}{2}. \end{cases} \tag{23}$$

IV. Time-Domain Analysis of the IPT System With a Detuned Secondary Side

As shown in (15) and (22), there is an imaginary part for the equivalent input impedance of the rectifier Z_{rec} when C_s is tuned with L_s at the operating frequency of the system, no matter in CCM or DCM mode. The imaginary part of Z_{rec} will cause reactive components to the system, thus lowering the PTE.

In this chapter, a detuned condition of the secondary side will be modeled and discussed, analyzing the possibility of decreasing the reactive components caused by Z_{rec}.

In an IPT system with a detuned secondary side, the value of C_s can be determined by

$$\omega_0 L_s = \frac{1}{\omega_0 C_s}, \quad \omega_0 = \delta\omega,\ \delta \neq 1 \tag{24}$$

where ω is the angular frequency of the system, and δ is the detuning coefficient of the secondary side. An overdetuned secondary side will bring lots of harmonics to the system and lower the PTE. Therefore, the range of δ is between 0.5 and 2 in this article.

The operating modes of the detuned secondary side of the IPT system can also be divided into three states (states 1, 2, 3 as shown in Fig. 3), the same with the tuned one. Next, the TDA method will be used to analyze the CCM and DCM of the system.

A. Continuous Conduction Mode (CCM)

In CCM mode, the waveforms of the secondary side can be depicted with Fig. 4, same with the tuned condition. The induced voltage in the secondary side u_s can be assumed as (8).

Next, the full cycle of the waveforms in Fig. 4 will be analyzed in two parts separated by π/ω.

1) $0 < t \leq \pi/\omega$: During this half of the cycle, the waveforms correspond to state 1 of Fig. 3. The state-space equation of the system can be derived as

$$\dot{\boldsymbol{x}}(t) = \boldsymbol{A}\boldsymbol{x}(t) + \boldsymbol{B}\boldsymbol{u}(t) \tag{25a}$$

where

$$\dot{\boldsymbol{x}}(t) = \begin{bmatrix} i_L(t) \\ u_C(t) \end{bmatrix},$$

$$\boldsymbol{A} = \begin{bmatrix} 0 & -\frac{1}{L_s} \\ \frac{1}{C_s} & 0 \end{bmatrix}, \quad \boldsymbol{B} = \begin{bmatrix} \frac{1}{L_s} & m\frac{1}{L_s} \\ 0 & 0 \end{bmatrix},$$

$$\boldsymbol{u}(t) = \begin{bmatrix} U_s\sin(\omega t+\theta) \\ U_o \end{bmatrix}, \quad U_o = U_{RL} + 2V_{d\_f} \tag{25b}$$

where U_{RL} is voltage of the load, V_{d_f} is the forward voltage of the diodes, and $m = -1$.

Equation (25) can be solved by

$$\boldsymbol{x}(t) = \boldsymbol{\Phi}(t)\boldsymbol{x}(0) + \int_0^t \boldsymbol{\Phi}(t-\tau)\mathbf{B}\boldsymbol{u}(\tau)\mathrm{d}\tau \tag{26a}$$

where

$$\boldsymbol{\Phi}(t) = \begin{bmatrix} \cos(\omega_0 t) & -\frac{1}{\omega L_s}\sin(\omega_0 t) \\ \omega L_s \sin(\omega_0 t) & \cos(\omega_0 t) \end{bmatrix},$$

$$\boldsymbol{x}(0) = \begin{bmatrix} 0 \\ u_C(0) \end{bmatrix}. \tag{26b}$$

Equation (26) can be calculated as

$$\boldsymbol{x}(t) = \begin{bmatrix} U_s F_1(t)/(\delta\omega L_s) \\ U_s F_2(t) \end{bmatrix} \tag{27}$$

where $F_1(t)$ and $F_2(t)$ is shown in (28) shown at the bottom of the next page.

According to antisymmetry property

$$\boldsymbol{x}\left(\frac{\pi}{\omega}\right) = -\boldsymbol{x}(0) = \begin{bmatrix} 0 \\ -G_{c0}U_s \end{bmatrix}. \tag{29}$$

The current in load is

$$I_o = \frac{\omega}{\pi}\int_0^{\frac{\pi}{\omega}} i(t)dt = U_s F_3/(\delta^2\pi\omega L_s) \tag{30}$$

where F_3 is shown in (28).

According to (29) and (30), the value of θ, G, and G_{c0} can be derived by solving

$$\begin{cases} F_1(\pi/\omega) = 0 \\ F_2(\pi/\omega) = -G_{c0} \\ F_3 = \delta^2\pi G/\beta. \end{cases} \tag{31}$$

2) $\pi/\omega < t < 2\pi/\omega$: During this half of the cycle, the waveforms correspond to state 2 of Fig. 3. The state-space equation of the system can also be written as (25), same as state 1 except that $m = 1$. The deduction of the state equation is similar with the first half of the cycle, and we would not elaborate it here to save space of the article.

During the full cycle, $i_L(t)$ can be derived as

$$i_L(t)=\begin{cases} U_sF_1(t)/(\delta\omega L_s) & t\in[0,\pi/\omega] \\ -U_sF_1(t-\frac{\pi}{\omega})/(\delta\omega L_s) & t\in(\pi/\omega,2\pi/\omega]. \end{cases} \tag{32}$$

As a square wave, $u_r(t)$ can be written as (10).

The fundamental components of i_L and u_r are in same form with (11), of which the coefficients can be derived with

$$\begin{cases} a_i=U_s\Lambda_1(\delta,\theta)/(\delta\pi\omega L_s) \\ b_i=U_s\Lambda_2(\delta,\theta)/(\delta\pi\omega L_s) \\ a_u=0 \\ b_u=4GU_s/\pi \end{cases} \tag{33}$$

where

$$\begin{cases} \Lambda_1(\delta,\theta)=\int_0^{\pi}F_1(t)\cos(\omega t)d\omega t \\ \qquad\qquad -\int_{\pi}^{2\pi}F_1(t-\frac{\pi}{\omega})\cos(\omega t)d\omega t \\ \Lambda_2(\delta,\theta)=\int_0^{\pi}F_1(t)\sin(\omega t)d\omega t \\ \qquad\qquad -\int_{\pi}^{2\pi}F_1(t-\frac{\pi}{\omega})\sin(\omega t)d\omega t. \end{cases} \tag{34}$$

Considering that $a_i<0$ (which will be discussed in the Appendix), the real and imaginary part of the equivalent input impedance of the rectifier can be derived by

$$\begin{cases} R_{\text{rec}}=\sqrt{\frac{a_u^2+b_u^2}{a_i^2+b_i^2}}\cos\left[acr\tan\frac{b_u}{a_u}-\left(\pi-acr\tan\frac{b_i}{a_i}\right)\right] \\ X_{\text{rec}}=\sqrt{\frac{a_u^2+b_u^2}{a_i^2+b_i^2}}\sin\left[acr\tan\frac{b_u}{a_u}-\left(\pi-acr\tan\frac{b_i}{a_i}\right)\right]. \end{cases} \tag{35}$$

Accordingly, R_{rec_β} and X_{rec_β} can be derived as

$$\begin{cases} R_{\text{rec}\_\beta}=4\delta G\Lambda_2(\delta,\theta)/[\Lambda_1(\delta,\theta)^2+\Lambda_2(\delta,\theta)^2] \\ X_{\text{rec}\_\beta}=-4\delta G\Lambda_1(\delta,\theta)/[\Lambda_1(\delta,\theta)^2+\Lambda_2(\delta,\theta)^2]. \end{cases} \tag{36}$$

By combining (28), (34), and (36), it can be deduced that R_{rec_β} and X_{rec_β} are only related to δ and β.

B. Discontinuous Conduction Mode (DCM)

In DCM mode, the waveforms of the secondary side can be depicted with Fig. 5, same with the tuned condition.

Depending on the state of $i_L(t)$, the operating modes of the system can be divided into four stages:

1) $0<\text{t}\le\varphi/\omega$: During this stage, the waveforms correspond to state 3 of Fig. 3, and u_c is constant because there is no current flowing through C_s, thus

$$\boldsymbol{x}(t)=\begin{bmatrix}0\\ G_{c0}U_s\end{bmatrix}. \tag{37}$$

When $t=\varphi/\omega$

$$u_r\left(\frac{\varphi}{\omega}\right)=U_o=U_s\sin(\varphi+\theta)-u_c(0)\ . \tag{38}$$

2) $\varphi/\omega<\text{t}\le\pi/\omega$: During this stage, the waveform corresponds to state 1 of Fig. 3, and the state-space equation is the same with (25), which can be solved by

$$\begin{aligned}\boldsymbol{x}(t)&=\boldsymbol{\Phi}(t)\boldsymbol{x}\left(\frac{\varphi}{\omega}\right)+\int_{\varphi/\omega}^{t}\boldsymbol{\Phi}(t-\tau)\boldsymbol{B}\boldsymbol{u}(\tau)d\tau \\ &=\begin{bmatrix}U_sF_4(t)/(\delta\omega L_s)\\ U_sF_5(t)\end{bmatrix}\end{aligned} \tag{39}$$

where $F_4(t)$ and $F_5(t)$ is shown in (40) at the bottom of the next page.

The current in load is

$$I_o=\frac{\omega}{\pi}\int_0^{\frac{\pi}{\omega}}i(t)dt=\frac{U_s}{\delta^2\pi\omega L_s}F_6 \tag{41}$$

where F_6 is shown in (40).

According to (38) and (41), the value of φ, θ, and G can be derived by solving

$$\begin{cases} F_4(\pi/\omega)=0 \\ F_5(\pi/\omega)=-G_{c0} \\ F_6=\delta^2\pi G/\beta. \end{cases} \tag{42}$$

3) $\pi/\omega<\text{t}\le(\pi+\varphi)/\omega$: During this stage, the waveforms correspond to state 3 of Fig. 3, and u_c remains constant because there is no current flowing through C_s, thus $\boldsymbol{x}(t)$ can be described with

$$\boldsymbol{x}(t)=\begin{bmatrix}0\\ -G_{c0}U_s\end{bmatrix}. \tag{43}$$

4) $(\pi+\varphi)/\omega<\text{t}\le2\pi/\omega$: During this stage, the waveforms correspond to state 2 of Fig. 3. The state-space equation of the system can also be written as (25), same as stage 1 except that $m=1$. The deduction of the state equation is similar with stage 1.

During the full cycle, $i_L(t)$ can be derived as

$$i_L(t)=\begin{cases} 0 & t\in[0,\ \varphi/\omega] \\ \frac{U_s}{\delta\omega L_s}F_4(t) & t\in(\varphi/\omega,\ \pi/\omega] \\ 0 & t\in(\pi/\omega,(\pi+\varphi)/\omega] \\ -\frac{U_s}{\delta\omega L_s}F_4(t-\frac{\pi}{\omega}) & t\in((\pi+\varphi)/\omega,2\pi/\omega]. \end{cases} \tag{44}$$

According to (38), $u_r(t)$ can be written as

$$u_r(t)=\begin{cases} U_s[\sin(\omega t+\theta)-G_{c0}] & t\in[0,\varphi/\omega] \\ GU_s & t\in(\varphi/\omega,\pi/\omega] \\ U_s[\sin(\omega t+\theta)+G_{c0}] & t\in(\pi/\omega,(\pi+\varphi)/\omega] \\ -GU_s & t\in((\pi+\varphi)/\omega,2\pi/\omega]. \end{cases} \tag{45}$$

$$\begin{cases} F_1(t)=\ \gamma\cos(\omega t+\theta)+\delta\gamma\sin\theta\sin(\delta\omega t)-\gamma\cos\theta\cos(\delta\omega t)-G\sin(\delta\omega t)-G_{c0}\sin(\delta\omega t) \\ F_2(t)=\ \delta\gamma\sin(\omega t+\theta)-\delta\gamma\sin\theta\cos(\delta\omega t)-\gamma\cos\theta\sin(\delta\omega t)+G\cos(\delta\omega t)-G+G_{c0}\cos(\delta\omega t) \\ F_3=-\delta\gamma\cos(\delta\pi)\sin\theta-\delta\gamma\sin\theta-\gamma\sin(\delta\pi)\cos\theta+(G+G_{c0})(\cos\delta\pi-1) \\ \gamma=\delta/(\delta^2-1) \end{cases} \tag{28}$$

The coefficients in fundamental components of $i_L(t)$ and $u_r(t)$ can be derived with

$$\begin{cases} a_i = U_s\Pi_1(\delta,\varphi,\theta)/(\delta\pi\omega L_s) \\ b_i = U_s\Pi_2(\delta,\varphi,\theta)/(\delta\pi\omega L_s) \\ a_u = U_s\Pi_3(\varphi,\theta)/(2\pi) \\ b_u = U_s\Pi_4(\varphi,\theta,G)/(2\pi) \end{cases} \tag{46}$$

where

$$\begin{cases} \Pi_1(\delta,\varphi,\theta) = \int_{\varphi}^{\pi} F_4(t)\cos(\omega t)d\omega t \\ \qquad\qquad -\int_{\pi+\varphi}^{2\pi} F_4(t-\frac{\pi}{\omega})\cos(\omega t)d\omega t \\ \Pi_2(\delta,\varphi,\theta) = \int_{\varphi}^{\pi} F_4(t)\sin(\omega t)d\omega t \\ \qquad\qquad -\int_{\pi+\varphi}^{2\pi} F_4(t-\frac{\pi}{\omega})\sin(\omega t)d\omega t \\ \Pi_3(\varphi,\theta) = 2\varphi\sin\theta + \cos(2\varphi+\theta) - \cos\theta \\ \Pi_4(\varphi,\theta,G) = 2\varphi\cos\theta + \sin(2\varphi+\theta) + 3\sin\theta \\ \qquad\qquad -4\sin(\varphi+\theta) + 8G. \end{cases} \tag{47}$$

Considering that a_i, $a_u < 0$ (which will be discussed in the Appendix), the real and imaginary part of the equivalent input impedance of the rectifier can be derived, which is in same form with (21).

Accordingly, R_{rec_β} and X_{rec_β} can be derived as

$$\begin{cases} R_{rec\_\beta} = \frac{\delta}{2}\sqrt{\frac{\Pi_3(\varphi,\theta)^2+\Pi_4(\varphi,\theta,G)}{\Pi_1(\delta,\varphi,\theta)^2+\Pi_2(\delta,\varphi,\theta)^2}}\cos(\arctan\frac{\Pi_2(\delta,\varphi,\theta)}{\Pi_1(\delta,\varphi,\theta)} \\ \qquad -\arctan\frac{\Pi_4(\varphi,\theta,G)}{\Pi_3(\varphi,\theta)}) \\ X_{rec\_\beta} = \frac{\delta}{2}\sqrt{\frac{\Pi_3(\varphi,\theta)^2+\Pi_4(\varphi,\theta,G)}{\Pi_1(\delta,\varphi,\theta)^2+\Pi_2(\delta,\varphi,\theta)^2}}\sin(\arctan\frac{\Pi_2(\delta,\varphi,\theta)}{\Pi_1(\delta,\varphi,\theta)} \\ \qquad -\arctan\frac{\Pi_4(\varphi,\theta,G)}{\Pi_3(\varphi,\theta)}). \end{cases} \tag{48}$$

By combining (40), (47), and (48), it can be deduced that R_{rec_β} and X_{rec_β} are only related to δ and β.

Besides, by assuming $\varphi = 0$, the critical condition between CCM and DCM can be derived as

$$\begin{cases} \theta = \delta[\csc(\delta\pi) + \cot(\delta\pi)] \\ \beta = \pi/2. \end{cases} \tag{49}$$

C. Overall Analysis of the Modeling of Secondary Side

Based on the modeling of secondary side in tuned and detuned conditions in Sections III and IV, the parameters featuring the models in CCM (θ, G, and G_{c0}) and DCM (φ, θ, and G) can be derived, as shown in Fig. 6. The value of θ [Fig. 6(a)], ranging from $-\pi$ to π, decreases with the increase of both δ and β. Another noteworthy point is that when δ is large enough ($\delta = 2$, for example), the influence of β on θ is very limited. Also, the "zero curve" of θ is perpendicular to the horizontal axis at $\delta = 1$ in CCM ($\beta < \pi/2$) and leans to the field of $\delta < 1$ in DCM ($\beta \geqslant \pi/2$), which indicates that the TDA method can depict the DCM state more accurately compared with FHA method which assumes θ as zero in DCM. Fig. 6(b) shows the value of G_{c0}, which is negative for all the given δ and β. The absolute value of G_{c0} decreases with the increase of β; for a specific β, it increases first and then decreases with the increase of δ and reaches the maximum value for a value of δ larger than 1. The amplitude of G_{c0} can be huge when β is small and δ is close to 1, which should be avoided considering the voltage stress on the capacitor. Fig. 6(c) shows the value of φ in DCM, which increases with the increase of both δ and β. For a light load (a large β), a large δ means a deep DCM state, which transfers little power and is adverse to the system. It is also noteworthy that when β is small enough (1.6, for example), the influence of δ on φ is very limited. Fig. 6(d) shows the value of G. The value of G increases with β; for a specific β, it increases first and then decreases with the increase of δ and reaches the maximum value for a value of δ larger than 1 ($\beta > 0.5$). According to the gain larger or smaller than tuned condition, the figure is divided into two parts: higher gain zone (shaded area) and lower gain zone. In the higher gain zone, a detuned system outperforms the tuned one.

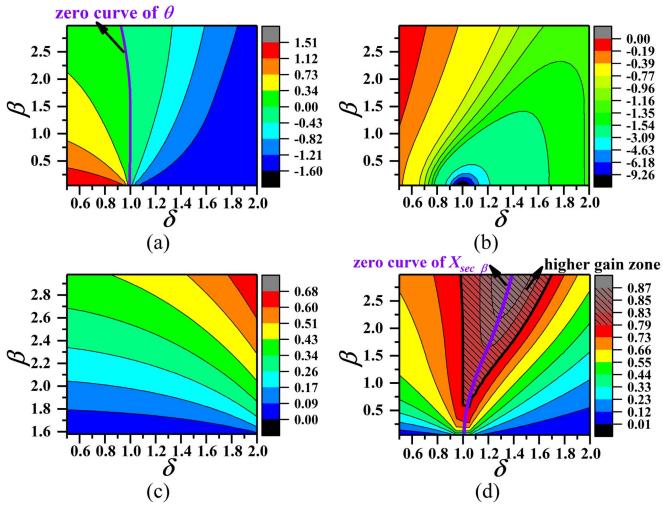

Fig. 6. Relation of θ, G_{c0}, φ, and G with δ and β.

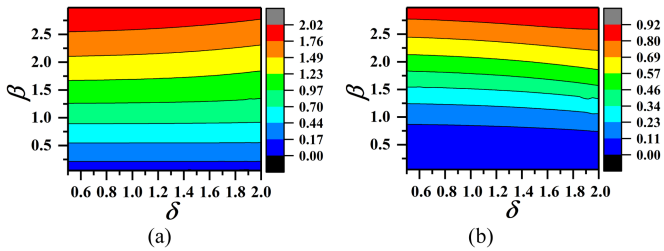

Fig. 7. Relation of R_{rec_β} and X_{rec_β} with δ and β. (a) R_{rec_β} (b) X_{rec_β}.

The relation of R_{rec_β} and X_{rec_β} with δ and β is depicted in Fig. 7(a) and (b), which shows that R_{rec_β} and X_{rec_β} are both proportional to β. The influence of δ on R_{rec_β} and X_{rec_β}

$$\begin{cases} F_4(t) = \gamma\cos(\omega t+\theta) + (\delta\gamma-1)\sin(\varphi+\theta)\sin(\delta\omega t-\delta\varphi) - \gamma\cos(\varphi+\theta)\cos(\delta\omega t-\delta\varphi) \\ F_5(t) = \delta\gamma\sin(\omega t+\theta) + (1-\delta\gamma)\sin(\varphi+\theta)\cos(\delta\omega t-\delta\varphi) - \gamma\cos(\varphi+\theta)\sin(\delta\omega t-\delta\varphi) - G \\ F_6 = -\sin(\varphi+\theta) - \delta\gamma\sin\theta + (1-\delta\gamma)\sin(\varphi+\theta)\cos(\delta\pi-\delta\varphi) - \gamma\cos(\varphi+\theta)\sin(\delta\pi-\delta\varphi) \end{cases} \tag{40}$$

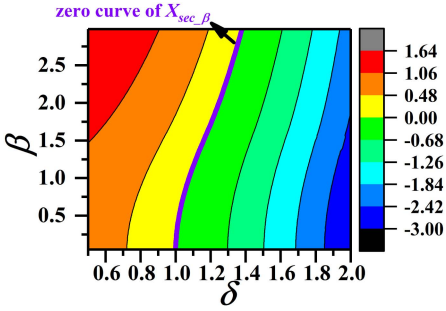

Fig. 8. Relation of X_{sec_β} with δ and β.

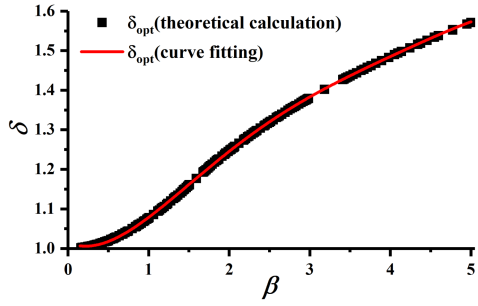

Fig. 9. Relation of β with δ_{opt}.

are very limited for a specific β. When $\beta > 1$, however, it can be noted that R_{rec_β} decreases and X_{rec_β} increases with the increase of δ.

V. Efficiency Improvement of IPT System by Detuning Design of the Secondary Side

As is discussed in Section IV, the equivalent input impedance of the rectifier will be influenced by δ, indicating that the reactive components in the secondary side can be compensated. In this chapter, the PTE improvement of the detuning in secondary side will be analyzed quantitatively, and the parameters of the *LCC* network will also be designed.

A. Compensation of the Reactive Components in the Secondary Side by Designing of δ

The input impedance of the secondary side (Z_{sec}) can be calculated with

$$Z_{\mathrm{sec}} = R_s + R_{\mathrm{rec}} + j[(1-\delta^2)\omega L_s + X_{\mathrm{rec}}]. \tag{50}$$

The ratio of X_{sec} (the imaginary part of Z_{sec}) with ωL_s is

$$X_{\mathrm{sec}\_\beta} = 1 - \delta^2 + X_{\mathrm{rec}\_\beta}. \tag{51}$$

The relation of X_{sec_β} with δ and β is shown in Fig. 8, which shows that X_{sec_β} is mainly determined by δ, and X_{sec} turns from an inductive impedance to a capacitive one with the increase of δ. A "zero curve" of X_{sec_β} is drawn in Fig. 8, which implies that for a specific value of β, the value of δ can be designed to compensate for the reactive components, we define this value of δ as δ_{opt}. Also, the "zero curve" of X_{sec_β} is drawn in the figure of G–δ, β relation [Fig. 6(d)], showing that the output voltage gain can be maximum by optimum design of δ.

The relation of β and δ_{opt} is shown in Fig. 9. To facilitate the optimum design of δ, the curves in Fig. 9 are approximated with curve fitting method. After curve fitting, the relation of $\delta_{\mathrm{opt}}-\beta$ can be approximated as

$$\begin{aligned}\delta_{\mathrm{opt}} \approx\ & -0.0008281\beta^5 + 0.01354\beta^4 - 0.08258\beta^3 \\ & + 0.2169\beta^2 - 0.08334\beta + 1.015.\end{aligned} \tag{52}$$

TABEL I
Parameters of the System

Parameter	Value
f/kHz	50
U_d/V	200
C_d/μF	150
C_L/μF	200
R_L/Ω	10–200
L_p/μH	238.18
L_s/μH	129.46
R_{LP}/Ω	0.187
R_{LS}/Ω	0.123
M/μH	52.89

B. Analysis of PTE of the System

According to (5) and (7), the PTE of an IPT system is

$$\eta = \frac{1}{1 + \frac{1}{2\omega L_s}\left(\frac{1}{\mu^2}R_{LP}\Delta_1 + R_{LS}\Delta_2\right)} \tag{53}$$

where

$$\begin{cases} \Delta_1 = \beta/G^2 \\ \Delta_2 = \frac{\omega\beta}{\pi G^2}\int_0^{\pi/\omega}\left[\frac{i_L(t)\omega L_s}{U_s}\right]^2 dt \\ \mu = M/L_s. \end{cases} \tag{54}$$

From (9), (16), (32), and (44), it can be derived that Δ_1 and Δ_2 can be determined by β; considering that L_s, R_{LP}, and R_{LS} are the intrinsic parameters of the system, we can conclude that η can be determined by μ and β. Based on parameters in Table I, the efficiency of the tuned system and detuned system are calculated separately. For the detuned system, the value of δ_{opt} for a specific β [calculated with (52)] is used in the process of calculation. Fig. 10(a) and (b) shows the relation of the PTE with μ and β in tuned and detuned conditions, separately. The high PTE zone (where PTE $\geq$ 90%) is labeled with shadow both in Fig. 10(a) and (b), indicating that the detuning design widens the range of high-PTE zone, especially for the large value of β. In Fig. 10(c), the ratio of PTE for detuned and tuned system ($\eta_{\mathrm{detuned}}/\eta_{\mathrm{tuned}}$) is depicted. In most circumstances, $\eta_{\mathrm{detuned}}/\eta_{\mathrm{tuned}} \geq 1$, showing that the PTE can be improved for a wide range of μ and β. When there is strong coupling among the coupling coils ($\mu > 0.4$), the PTE of detuned and tuned system are close; with the decrease of μ, $\eta_{\mathrm{detuned}}/\eta_{\mathrm{tuned}}$ is increased, especially for the large value of β. This phenomenon indicates

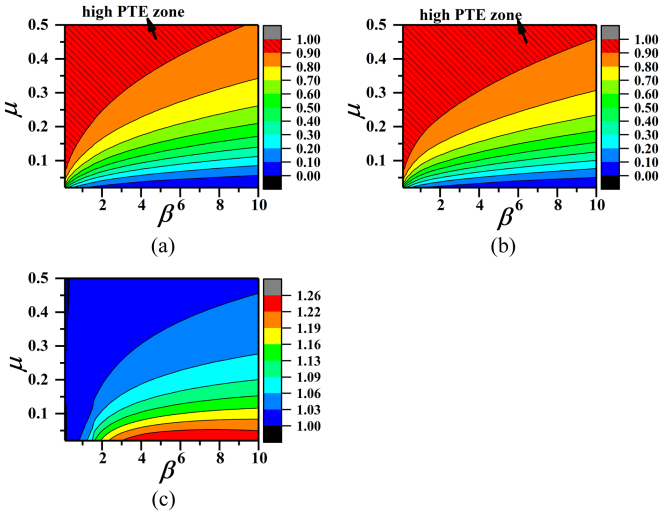

Fig. 10. Comparison of η_{detuned} and η_{tuned}. (a) PTE in tuned condition. (b) PTE in detuned condition. (c) $\eta_{\text{detuned}}/\eta_{\text{tuned}}$.

that in the circumstance of misalignment, the advantage of detuned design over tuned one can be more obvious.

C. Parameter Design of the LCC Network in the Primary Side for Fixed Load

To verify the analysis of PTE in practice, the parameters of the *LCC* network in the primary side should be determined based on the tuned or detuned conditions of the secondary side.

According to (1), the key to design the parameters of *LCC* network is to solve X_p (the value of α can be designed based on X_p, and will not be elaborated in this article). In this article, we will discuss the designing of X_p for fixed and variable load separately.

For a constant load, the design of X_p should follow the steps as follows.

Step 1: Calculate U_{RL} with

$$U_{RL} = \sqrt{P_{o\_n} R_{LN}} \tag{55}$$

where P_{o_n} is the nominal output power of the system and R_{LN} is the nominal load.

Step 2: Calculate β with (14) and determine the operating mode of the rectifier with (23) or (49): if $\beta < \pi/2$, the rectifier is in CCM; if $\beta \geq \pi/2$, the rectifier is in DCM.

Step 3: Calculate U_s with

$$U_s = G(U_{RL} + 2V_{d\_f}). \tag{56}$$

The derivation of G depends on whether the secondary side is in tuned or detuned condition and the operating mode of the rectifier: if the secondary side is in tuned condition and the rectifier is in CCM, $G = \pi/4$; if the secondary side is in tuned condition and the rectifier is in DCM, G can be calculated by solving (18); if the secondary side is in detuned condition and the rectifier is in CCM, G can be calculated by solving (31); and if the secondary side is in detuned condition and the rectifier is in DCM, G can be calculated by solving (42).

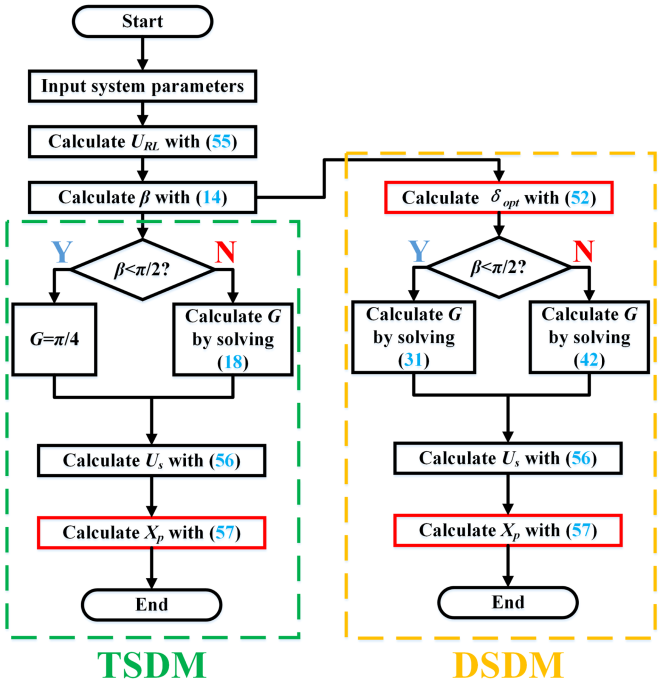

Fig. 11. Flowchart of parameter designing process with TSDM and DSDM.

Step 4: Calculate X_p by combining (2) and (5), i.e.,

$$X_p = \frac{4\omega M U_d}{\pi U_s}. \tag{57}$$

A flowchart of the designing process is shown in Fig. 11, where "TSDM" means tuned secondary-side-based design method, while "DSDM" means detuned secondary-side-based design method.

D. Parameter Design of the LCC Network in the Primary Side for Variable Load (Taking Battery Charging as an Example)

As shown in Fig. 1, the charging profile of a battery usually contains CC and CV stage, and the equivalent load varies with the charging. A switch-controlled capacitor can be used to change C_s to fit for δ_{opt}. The controlling of C_s can be realized by utilizing a switched controlled capacitor [34], which is not the main focus of this article, and will be studied in future.

To design X_p of a WPT system for battery charging, the whole charging process should be taken into consideration. Therefore, the energy transfer efficiency (ETE) is defined as

$$\eta = \int_{t_0}^{t_e} P_o(t)dt \Big/ \int_{t_0}^{t_e} P_{\text{in}}(t)dt \tag{58}$$

where t_0 and t_e are the starting and end time of the charging, separately. $P_o(t)$ and $P_{\text{in}}(t)$ are the output and input power of the WPT system at time t, separately.

Another noteworthy point for battery charging is the controlling techniques in the secondary side. The equivalent output impedance of the rectifier will be influenced by the dc–dc converter. In this article, a buck converter [45] is taken as an example.

For a specific duty ratio D of the buck converter, the voltage gain G can be derived as

$$G = U_b/(DU_s) \tag{59}$$

where U_b is the voltage of the battery.

The equivalent load of the battery is R_b, and the equivalent output impedance of the rectifier is

$$R_L = R_b/D^2. \tag{60}$$

According to the above analysis, X_p for battery charging can be designed with the following steps.

Step 1: Discretize the battery charging profile by measuring or simulating the charging process per time. Define the initial value, maximum value, and optimum value of X_p as X_{p_0}, X_{p_e}, and X_{p_opt}. Define the optimum ETE as $\mathrm{ETE}_{\_\max}$. To initialize the procedure, let $X_{p\_\mathrm{opt}} = X_{p\_0}$, $\mathrm{ETE}_{\_\max} = 0$.

Step 2: Input the first group of battery charging data, including U_b, I_b (charging current), and R_b. Calculate R_L with (60), where D is the initial value of the duty ratio.

Step 3: Calculate β with the same method for constant load.

Step 4: Calculate G, U_s, and δ_{opt} with the same method for constant load.

Step 5: Calculate G with (59), which may differ from the result of step 4, thus define it as G'. Calculate the absolute value of the difference between G and G', $|G-G'|$.

Step 6: Update the value of D, and loop steps 3–5 until D reaches its maximum value. After the loop, the minimum value of $|G-G'|$ can be obtained, and define it as $|G-G'|_{\_\min}$. If $|G-G'|_{\_\min}$ is larger than a specific value G_i(0.01, for example), denoting that the value of X_p does not fit, and X_p will be updated and return to step 2.

Step 7: Calculate the PTE with (7), where P_o can be derived with $P_o = U_bI_b$, I_p can be calculated with (2), and I_s can be derived by (32) or (44).

Step 8: Update the battery charging data and loop steps 2–6 until the last group of data.

Step 9: Calculate ETE with (58), and update $\mathrm{ETE}_{\_\max}$ and X_{p_opt} if the calculated ETE is larger than the old one.

Step 10: Update X_p and loop steps 2–8 until X_p reaches its maximum value.

A flowchart of the designing process for battery charging is shown in Fig. 12.

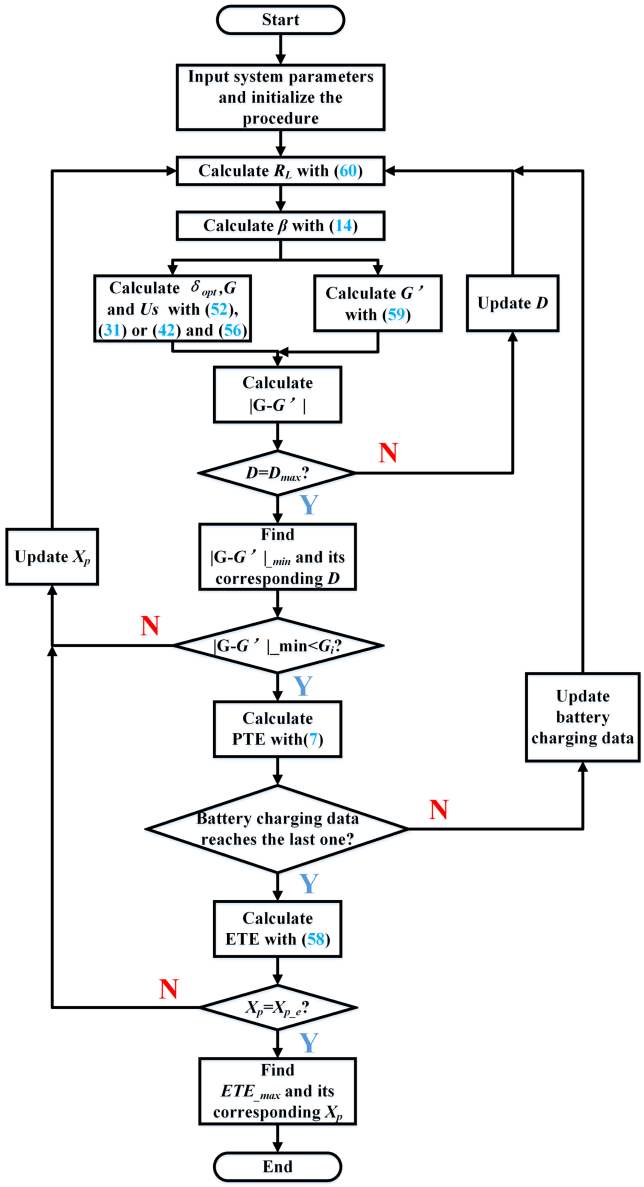

Fig. 12. Flowchart of parameter designing process for battery load.

VI. Simulation and Experimental Verification

To verify the proposed modeling and design method, simulation and experiments are conducted based on parameters in Table I. An experimental prototype is built as shown in Fig. 13, the primary side coil is 20-turn with the size of 35 cm × 35 cm, the secondary side coil is 13-turn with the size of 30 cm × 30 cm. Four IPW65R080 MOSFETs are used in the inverter and two IXYS DSEI 2X101 diode modules comprise the rectifier, a TI DSP TMS320F28335 is used as the controller.

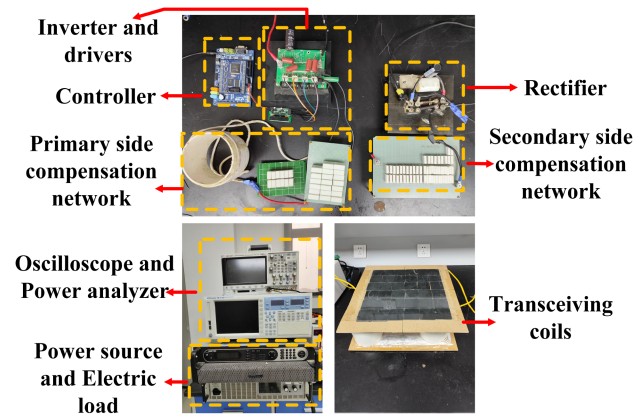

Fig. 13. Built experimental prototype.

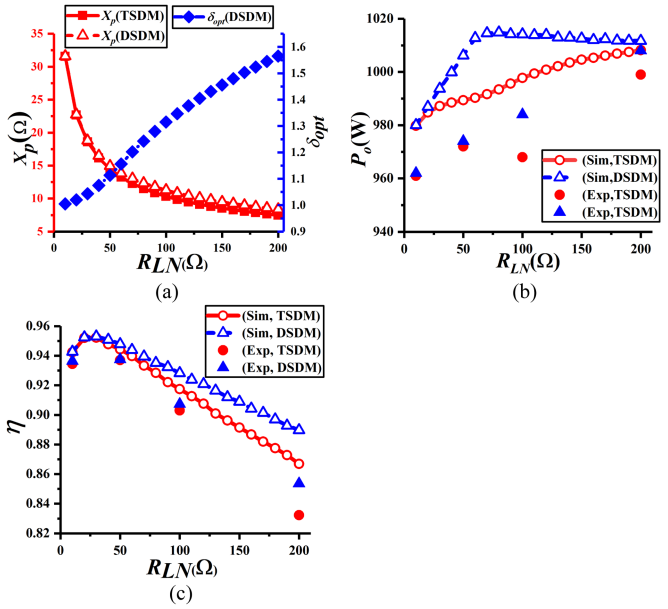

Fig. 14. Results of parameter design in simulation and experiments. (a) Designed X_p and δ_{opt}. (b) Output power. (c) PTE.

A. *Parameter Design for Fixed Load and Experimental Verification*

The parameters of *LCC* network in the primary side are designed based on a fixed nominal load (R_{LN}) ranging from 10–200 Ω and nominal power (P_{o_n}) of 1000 W with TSDM and DSDM, as shown in Fig. 14(a). As the figure shows, the value of X_p based on DSDM is slightly larger than that based on TSDM. This can help to partly explain the neglection of the losses in the compensation networks in (7). The value of δ_{opt} increases with R_{LN}. Fig. 14(b) and (c) shows the output power and PTE of the IPT system in the simulation and experiments, and the value of load 10, 50, 100, and 200 Ω were chosen in experiments to simplify the verification. The output power [Fig. 14(b)] of IPT system designed by DSDM is larger than that designed by TSDM. Noted that the output power deviates from the nominal power, no matter for DSDM or TSDM. The main reason is the ignorance of the parasitic resistance of components in modeling and designing of the system. The PTE [Fig. 14(c)] of the system based on DSDM is larger than that of TSDM in the whole range of load, and the gap increases with the load, which verifies the analysis in Section V.

B. *Verification of the Time-Domain Modeling With Experimental Waveforms*

Fig. 15 shows the waveforms of the input voltage and current of the rectifier (U_{rec}, I_{rec}) when *LCC*-S network is designed with DSDM. When $R_{LN} = 10$ and 50 Ω [Fig. 15(a) and (b)], the rectifier is in CCM, and the theoretical waveforms feature the experimental results very well. When $R_{LN} = 100\,\Omega$ [Fig. 15(c)], the rectifier is in DCM, and the theoretical waveforms also feature the experimental results well. When $R_{LN} = 200\ \Omega$ [Fig. 15(d)], the rectifier is in DCM, and there is a resonant

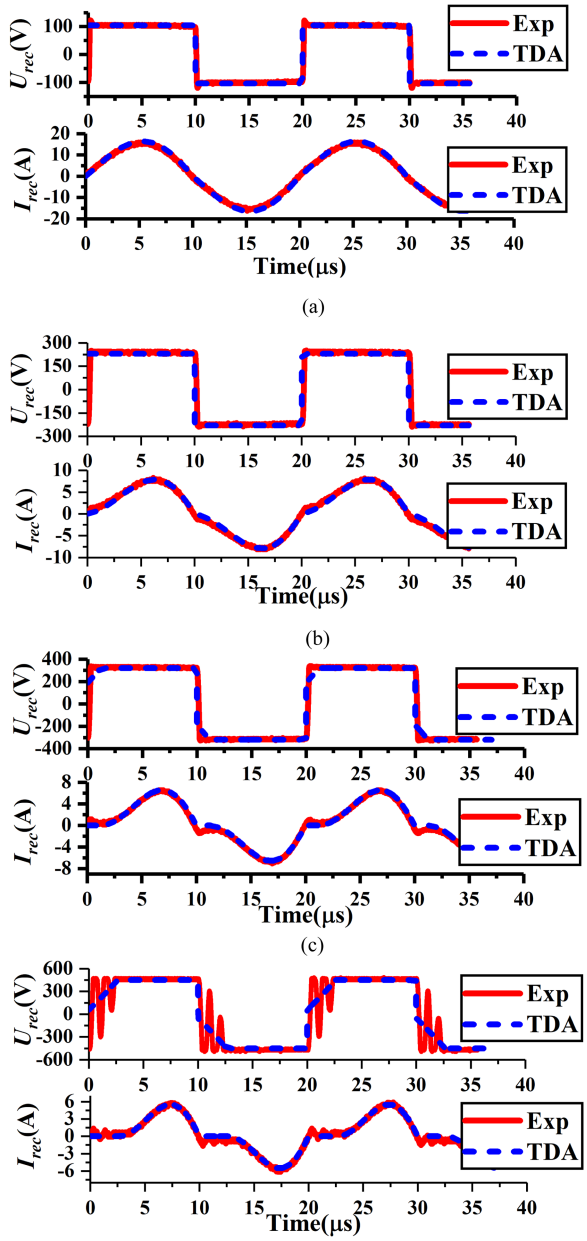

Fig. 15. Waveforms of U_{rec} and I_{rec} for DSDM. (a) R_{LN}= 10 Ω. (b) R_{LN}= 50 Ω. (c) R_{LN}= 100 Ω. (d) R_{LN}= 200 Ω.

superimposed on the waveform of U_{rec}, this is because a resonance takes place between L_s and the combination of C_s and the parasitic capacitance of the diodes [36]. In conclusion, the theoretical waveforms feature the experimental results very well.

C. *Performance Analysis in Condition of Misalignment and Load Variation*

To compare the performance of TSDM and DSDM in condition of misalignment (the mutual inductance *M* and coupling coefficient *k* with the misalignment distance is shown in Fig. 16) and load variation, experiments are conducted both in state of heavy ($R_{LN} = 50\,\Omega$) and light ($R_{LN} = 100\,\Omega$) nominal load, as shown in Fig. 17. With the misaligned distance of the coupling

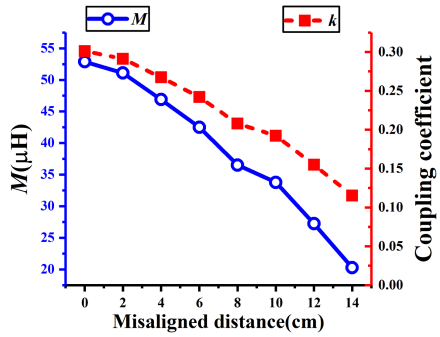

Fig. 16. Mutual inductance and coupling coefficient curves in misalignment.

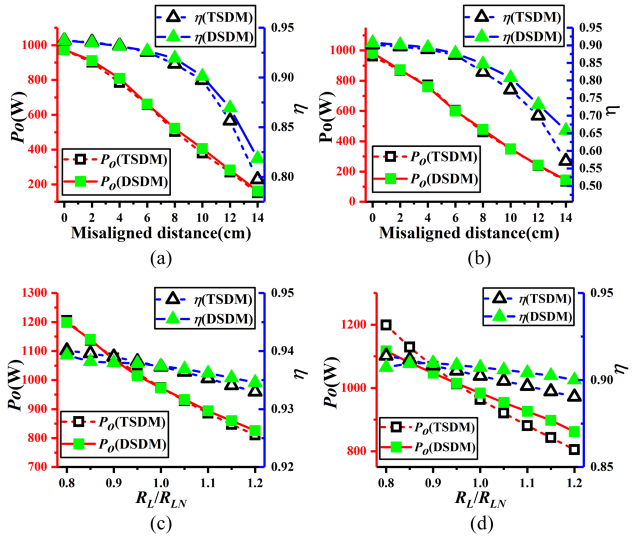

Fig. 17. Results of experiments in condition of misalignment and load variation. (a) M changes for R_{LN}= 50 Ω. (b) M changes for R_{LN}= 100 Ω. (c) R_L changes for R_{LN}= 50 Ω. (d) R_L changes for R_{LN}= 100 Ω.

coils increases from 0 to 14 cm, the output power of the IPT system with heavy [Fig. 17(a)] and light load [Fig. 17(b)] both decreases from 1000 W to less than 200 W, and there is hardly difference between TSDM and DSDM. The PTE, however, is quite different between TSDM and DSDM. With heavy load [Fig. 17(a)], the PTE based on TSDM decreases to less than 80%, while the PTE based on DSDM is higher than TSDM with the misalignment distance increases. With light load [Fig. 17(b)], the PTE based on DSDM is also higher than TSDM, and the difference rises with the misalignment distance. The value of β for R_{LN} = 50 and 100 Ω are 1.233 and 2.467, separately, and the PTE difference in the experiments agrees with the theoretical analysis shown in Fig. 10(c).

In the load-variation experiments, the load of the system varies from 0.8 to 1.2 times of the nominal load when the coils are fully aligned. With heavy load [Fig. 17(c)], there is hardly difference in the output power between TSDM and DSDM. The PTE of DSDM is slightly lower than TSDM when R_L/R_{LN} is lower than 1, and is slightly higher than TSDM when R_L/R_{LN} is higher than 1. With light load [Fig. 17(d)], the output power and PTE of DSDM is higher than that of TSDM when the load is lighter than the nominal load, but the difference may be reverse with a

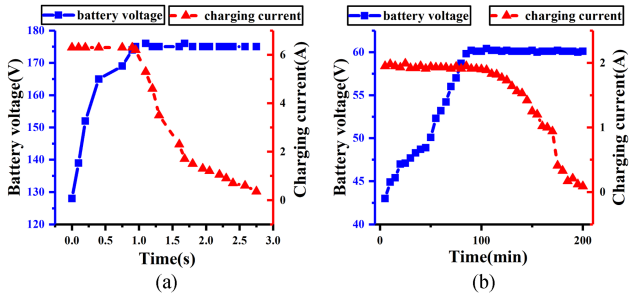

Fig. 18. Battery charging profiles in [46] and [47]. (a) Profile in [46]. (b) Profile in [47].

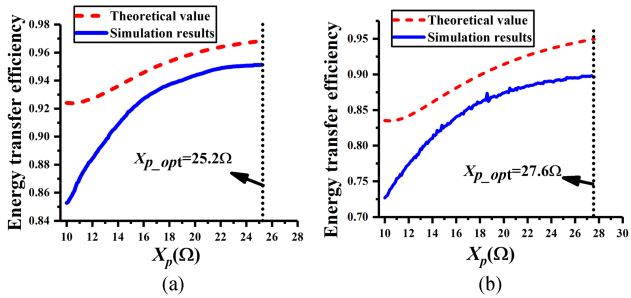

Fig. 19. ETE for [46] and [47]. (a) ETE for [46]. (b) ETE for [47].

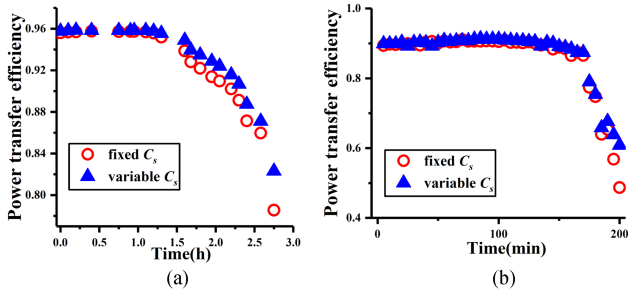

Fig. 20. PTE for [46] and [47] with the optimum value of X_p. (a) PTE for [46]. (b) PTE for [47].

heavier load. The PTE difference in the experiments agrees with the theoretical analysis shown in Fig. 10(c), where the difference of PTE increases with β.

D. Parameter Design for Battery Load and Simulation Verification

According to Section V-D, the parameter design for battery load should be based on the battery charging profile. In this article, however, the experimental setup for battery charging is lack due to the limitation of the laboratory. Instead, the proposed parameter design method is verified by using battery charging profile in the literature. Fig. 18 shows the charging profile in [46] and [47], respectively. It should be noted that the data shown in Fig. 18 are based on the figures in the literature, and has little difference with the original data, which will not influence the results of parameter designing.

The parameters of *LCC* network are designed based on the battery charging profile and other system parameters in [46] and [47]. The relation of ETE with X_p is shown in Fig. 19. Simulation

TABEL II
COMPARISON OF SECONDARY-SIDE DESIGNING METHODS

Literature	Compensation network	Designing method	Rectifier mode	UPF in the secondary side	Range of load	Power rate	PTE with fully aligned coils
[25]	SS	Detuning design	CCM	No	Constant voltage	60 W	–70%
[31]	*LCC*–*LCC*	Switched capacitor	CCM	No	5–50 Ω	400 W	Not mentioned
[32]	SS	Switched capacitor	Not mentioned	No	Not mentioned	650 W	91.2%
[33]	*LCC*-S	Switched capacitor	CCM	No	Fixed at 28.3 Ω	700 W	86.9%
[48]	*LCC*–TCN	Switched capacitor	CCM	No	Fixed at 28 Ω	Not mentioned	Not mentioned
[26]	*LCC*–LCC	Detuning design	CCM	No	Fixed at 40 Ω	1 kW	91.73%–95%
[43]	LS–SL	Dual shunt inductor	CCM and DCM	Nearly UPF	43–300 Ω	2.1 kW	86%–95.6%
[34]	SS	Switched capacitor	CCM	Nearly UPF	Fixed at 54.8 Ω	3.2 kW	95.68%–96.3%
Proposed	***LCC*-S**	**Detuning design and switching capacitor**	**CCM and DCM**	**UPF**	**50–200 Ω**	**1 kW**	**87.7%–93.5%**

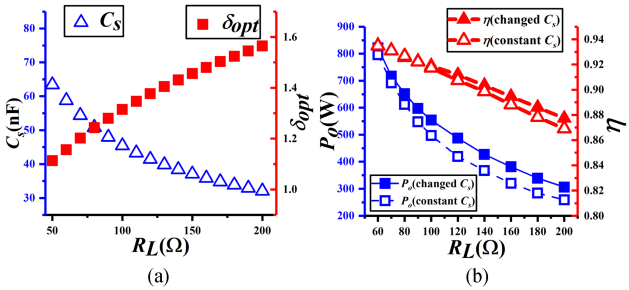

Fig. 21. Results of experiments with and without change of C_s. (a) C_s changing with δ_{opt}. (b) Output power.

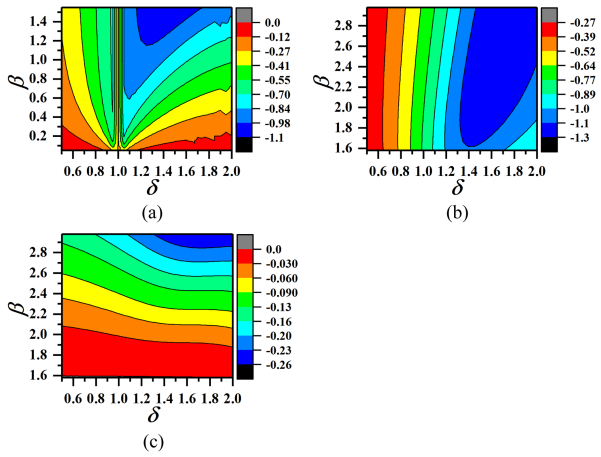

Fig. 22. Relation of a_i and a_u with δ and β. (a) a_i in CCM. (b) a_i in DCM. (c) a_u in DCM.

results agree with the theoretical values well, and in a specific range, the ETE increases with X_p. However, when X_p is larger than the optimum value, the duty ratio of the buck converter cannot meet the needs of output power, and such values of X_p should be given up. Finally, the optimum value of X_p for [46] and [47] are 25.2 and 27.6 Ω, respectively, and the highest ETE in simulation are 95.1% and 89.6%, respectively.

With the optimum value of X_p, the scatter plot of PTE during the whole charging procedure is shown in Fig. 20. The equivalent load of the battery will be light when the charging enters CV mode, thus leading the rectifier into DCM, and C_s will be regulated to realize UPF. In the CC charging stage, the PTE for fixed and variable C_s are close; while in the CV charging stage, the PTE for variable C_s is obviously higher than that of the fixed load.

E. Experimental Verification of the Variable C_s

To further verify the proposed parameter design method, the value of C_s is regulated according to δ_{opt} with the change of load in the experiments. Based on a system (based on the prototype in Fig. 13) of which the parameters are designed with DSDM for $R_{LN} = 50\ \Omega$, a load variation experiment is conducted. When the load varies from 50 to 200 Ω, the value of C_s is changed based on δ_{opt}, as shown in Fig. 21. The output power and PTE of the system are compared with the system with a constant value of C_s (based on δ_{opt} for $R_{LN} = 50\ \Omega$). The output power and PTE have been improved with the change of C_s.

The proposed designing method in this article is compared with the previous articles, as shown in Table II. Comparatively speaking, the detuned design method in this article can realize UPF in a wide range of load, while keeping a relatively high PTE and simple structure of the secondary side.

VIII. CONCLUSION

A detuning design method of the secondary side of an *LCC*-S based IPT system is proposed in this article to improve the PTE and realize UPF of the secondary side without adding any components. The state-space equation in time domain of the rectifier circuit both in CCM and DCM are analyzed, proving that the equivalent input impedance of the rectifier is inductive. By modeling of the detuned secondary side, it was found that the PTE of a detuned system is higher than a tuned system in most circumstances, especially when the coupling coils are highly misaligned or there is a light load. The parameters of the *LCC*-S network both for fixed and variable load are designed based on the detuned secondary side. The proposed modeling and designing method are verified with simulations and experiments.

APPENDIX

The value of a_i in CCM of the rectifier is shown in Fig. 22(a), from which it can be concluded that the sign of a_i is negative. The value of a_i and a_u in DCM of the rectifier is shown in Fig. 22(b) and (c), from which it can be concluded that the signs of a_i and a_u are both negative.

REFERENCES

[1] G. A. Covic and J. T. Boys, "Inductive power transfer," *Proc. IEEE*, vol. 101, no. 6, pp. 1276–1289, Jun. 2013.

[2] Z. Zhang, H. Pang, A. Georgiadis, and C. Cecati, "Wireless power transfer—An overview," *IEEE Trans. Ind. Electron.*, vol. 66, no. 2, pp. 1044–1058, Feb. 2019.

[3] D. Kim, A. Abu-Siada, and A. Sutinjo, "State-of-the-art literature review of WPT: Current limitations and solutions on IPT," *Elect. Power Syst. Res.*, vol. 154, pp. 493–502, 2018.

[4] P. Machura and Q. Li, "A critical review on wireless charging for electric vehicles," *Renewable Sustain. Energy Rev.*, vol. 104, pp. 209–234, 2019.

[5] P. K. Chittoor, B. Chokkalingam, and L. Mihet-Popa, "A review on UAV wireless charging: Fundamentals, applications, charging techniques and standards," *IEEE Access*, vol. 9, pp. 69235–69266, 2021.

[6] I. A. Mashhadi, M. Pahlevani, S. Hor, H. Pahlevani, and E. Adib, "A new wireless power-transfer circuit for retinal prosthesis," *IEEE Trans. Power Electron.*, vol. 34, no. 7, pp. 6425–6439, Jul. 2019.

[7] M. Ursino et al., "Hybrid planar Litz coil optimization for phone wireless power transfer," in *Proc. IEEE Appl. Power Electron. Conf. Expo.*, 2021, pp. 1560–1564.

[8] X. Zhu et al., "High-efficiency WPT system for CC/CV charging based on double-half-bridge inverter topology with variable inductors," *IEEE Trans. Power Electron.*, vol. 37, no. 2, pp. 2437–2448, Feb. 2022.

[9] F. Xu, S.-C. Wong, and C. K. Tse, "Overall loss compensation and optimization control in single-stage inductive power transfer converter delivering constant power," *IEEE Trans. Power Electron.*, vol. 37, no. 1, pp. 1146–1158, Jan. 2022.

[10] C. Ma, X. Qu, Y. Li, and J. Liu, "Single-stage active rectifier with wide impedance conversion ratio range for inductive power transfer system delivering constant power," *IEEE Trans. Power Electron.*, vol. 38, no. 6, pp. 7877–7890, Jun. 2023.

[11] A. C. Bagchi, A. Kamineni, R. A. Zane, and R. Carlson, "Review and comparative analysis of topologies and control methods in dynamic wireless charging of electric vehicles," *IEEE J. Emerg. Sel. Topics Power Electron.*, vol. 9, no. 4, pp. 4947–4962, Aug. 2021.

[12] D. Patil, M. K. McDonough, J. M. Miller, B. Fahimi, and P. T. Balsara, "Wireless power transfer for vehicular applications: Overview and challenges," *IEEE Trans. Transp. Electrific.*, vol. 4, no. 1, pp. 3–37, Mar. 2018.

[13] Z. She, S. Chen, Y. Chen, Y. Zhang, H. Li, and Y. Tang, "Efficiency analysis of LCC-S and S-S inductive power transfer considering switching device and component losses," in *Proc. IEEE 9th Int. Power Electron. Motion Control Conf.*, 2020, pp. 2956–2960.

[14] Y. Chen, H. Zhang, C.-S. Shin, K.-H. Seo, S.-J. Park, and D.-H. Kim, "A comparative study of S-S and LCC-S compensation topology of inductive power transfer systems for EV chargers," in *Proc. IEEE 10th Int. Symp. Power Electron. Distrib. Gener. Syst.*, 2019, pp. 99–104.

[15] W. X. Zhong and S. Y. R. Hui, "Maximum energy efficiency tracking for wireless power transfer systems," *IEEE Trans. Power Electron.*, vol. 30, no. 7, pp. 4025–4034, Jul. 2015.

[16] W. Zhong and S. Y. Hui, "Reconfigurable wireless power transfer systems with high energy efficiency over wide load range," *IEEE Trans. Power Electron.*, vol. 33, no. 7, pp. 6379–6390, Jul. 2018.

[17] W. Zhong and S. Y. R. Hui, "Maximum energy efficiency operation of series-series resonant wireless power transfer systems using on-off keying modulation," *IEEE Trans. Power Electron.*, vol. 33, no. 4, pp. 3595–3603, Apr. 2018.

[18] Z. Yan et al., "Fault-tolerant wireless power transfer system with a dual-coupled LCC-S topology," *IEEE Trans. Veh. Technol.*, vol. 68, no. 12, pp. 11838–11846, Dec. 2019.

[19] V.-B. Vu, D.-H. Tran, and W. Choi, "Implementation of the constant current and constant voltage charge of inductive power transfer systems with the double-sided *LCC* compensation topology for electric vehicle battery charge applications," *IEEE Trans. Power Electron.*, vol. 33, no. 9, pp. 7398–7410, Sep. 2018.

[20] F. Lu, H. Zhang, H. Hofmann, W. Su, and C. C. Mi, "A dual-coupled LCC-compensated IPT system with a compact magnetic coupler," *IEEE Trans. Power Electron.*, vol. 33, no. 7, pp. 6391–6402, Jul. 2018.

[21] Q. Zhu, L. Wang, Y. Guo, C. Liao, and F. Li, "Applying *LCC* compensation network to dynamic wireless EV charging system," *IEEE Trans. Ind. Electron.*, vol. 63, no. 10, pp. 6557–6567, Oct. 2016.

[22] Z. Yuan, M. Saeedifard, C. Cai, Q. Yang, P. Zhang, and H. Lin, "A misalignment tolerant design for a dual-coupled LCC-S-compensated WPT system with load-independent CC output," *IEEE Trans. Power Electron.*, vol. 37, no. 6, pp. 7480–7492, Jun. 2022.

[23] P. Deng, C. Tang, Y. Fan, M. Sun, Z. Liu, and X. Li, "A frequency regulation strategy for dynamic process noise suppression in LCC-S WPT systems," *IEEE Trans. Power Electron.*, vol. 37, no. 11, pp. 13978–13988, Nov. 2022.

[24] V. Yenil and S. Cetin, "An improved pulse density modulation control for secondary side controlled wireless power transfer system using LCC-S compensation," *IEEE Trans. Ind. Electron.*, vol. 69, no. 12, pp. 12762–12772, Dec. 2022.

[25] H. Feng, T. Cai, S. Duan, X. Zhang, H. Hu, and J. Niu, "A dual-side-detuned series–series compensated resonant converter for wide charging region in a wireless power transfer system," *IEEE Trans. Ind. Electron.*, vol. 65, no. 3, pp. 2177–2188, Mar. 2018.

[26] Y. Lu, T. Lyu, B. Yang, Y. Chen, and R. Mai, "Parameter design method for SS compensated dynamic wireless transfer system considering coils' parameters variations," in *Proc. IEEE 2nd China Int. Youth Conf. Elect. Eng.*, 2021, pp. 1–5.

[27] Y. Wei, F. Wu, and H. Liu, "Indirect control strategy of secondary charging voltage and current and transient analysis of LCC-S WPT system," *IEEE J. Emerg. Sel. Topics Power Electron.*, vol. 11, no. 2, pp. 2364–2376, Apr. 2023.

[28] X. Wang, J. Xu, M. Leng, H. Ma, and S. He, "A hybrid control strategy of LCC-S compensated WPT system for wide output voltage and ZVS range with minimized reactive current," *IEEE Trans. Ind. Electron.*, vol. 68, no. 9, pp. 7908–7920, Sep. 2021.

[29] S. Chen et al., "An operation mode selection method of dual-side bridge converters for efficiency optimization in inductive power transfer," *IEEE Trans. Power Electron.*, vol. 35, no. 10, pp. 9992–9997, Oct. 2020.

[30] Y. Chen, S. He, B. Yang, S. Chen, Z. He, and R. Mai, "Reconfigurable rectifier-based detuned series-series compensated IPT system for anti-misalignment and efficiency improvement," *IEEE Trans. Power Electron.*, vol. 38, no. 2, pp. 2720–2729, Feb. 2023.

[31] J. Wang, Z. Chang, B. Zhang, X. Yang, and H. Tang, "Analysis of ICPT system with LCC resonant topology based on the switch-controlled capacitor," in *Proc. IEEE Wireless Power Transfer Conf.*, 2020, pp. 178–182.

[32] J. Zhang, J. Zhao, Y. Zhang, and F. Deng, "A wireless power transfer system with dual switch-controlled capacitors for efficiency optimization," *IEEE Trans. Power Electron.*, vol. 35, no. 6, pp. 6091–6101, Jun. 2020.

[33] W. Li, G. Wei, C. Cui, X. Zhang, and Q. Zhang, "A double-side self-tuning LCC/S system using a variable switched capacitor based on parameter recognition," *IEEE Trans. Ind. Electron.*, vol. 68, no. 4, pp. 3069–3078, Apr. 2021.

[34] F. Grazian, T. B. Soeiro, and P. Bauer, "Inductive power transfer based on variable compensation capacitance to achieve an EV charging profile with constant optimum load," *IEEE J. Emerg. Sel. Topics Power Electron.*, vol. 11, no. 1, pp. 1230–1244, Feb. 2023.

[35] J. Jiang, K. Song, Z. Li, C. Zhu, and Q. Zhang, "System modeling and switching control strategy of wireless power transfer system," *IEEE J. Emerg. Sel. Topics Power Electron.*, vol. 6, no. 3, pp. 1295–1305, Sep. 2018.

[36] A. Safaee and K. Woronowicz, "Time-domain analysis of voltage-driven series–series compensated inductive power transfer topology," *IEEE Trans. Power Electron.*, vol. 32, no. 7, pp. 4981–5003, Jul. 2017.

[37] W. Li, H. Zhao, S. Li, J. Deng, T. Kan, and C. C. Mi, "Integrated *LCC* compensation topology for wireless charger in electric and plug-in electric vehicles," *IEEE Trans. Ind. Electron.*, vol. 62, no. 7, pp. 4215–4225, Jul. 2015.

[38] Y. Guo, L. Wang, Y. Zhang, S. Li, and C. Liao, "Rectifier load analysis for electric vehicle wireless charging system," *IEEE Trans. Ind. Electron.*, vol. 65, no. 9, pp. 6970–6982, Sep. 2018.

[39] Y. Guo, Y. Zhang, Q. Bo, Z. Liu, J. Meng, and L. Wang, "Approximate linearization of rectifier load in wireless power transfer systems," in *Proc. IEEE PELS Workshop Emerg. Technol., Wireless Power Transfer*, 2020, pp. 74–78.

[40] S. Li, F. Li, R. Zhang, C. Tao, and L. Wang, "Accurate modeling, design and load estimation of LCC-S based WPT system with a wide range of load," *IEEE Trans. Power Electron.*, vol. 38, no. 10, pp. 11763–11775, Oct. 2023.

[41] N. A. Keeling, G. A. Covic, and J. T. Boys, "A unity-power-factor IPT pickup for high-power applications," *IEEE Trans. Ind. Electron.*, vol. 57, no. 2, pp. 744–751, Feb. 2010.

[42] X. Qu, Y. Jing, J. Lian, S.-C. Wong, and C. K. Tse, "Design for continuous-current-mode operation of inductive-power-transfer converters with load-independent output," *Inst. Eng. Technol. Power Electron.*, vol. 12, no. 10, pp. 2458–2465, 2019.

[43] S. Luo, Z. Yao, Z. Zhang, G. Li, X. Zhang, and H. Ma, "A dual shunt inductor compensated IPT system with nearly unity power factor for wide load range and misalignment tolerance," *IEEE Trans. Ind. Electron.*, vol. 69, no. 10, pp. 10001–10013, Oct. 2022.
[44] S. Li, Y. Guo, C. Tao, F. Li, L. Wang, and Q. Bo, "Analysis of the input impedance of the rectifier and design of LCC compensation network of the dynamic wireless power transfer system," *Inst. Eng. Technol. Power Electron.*, vol. 12, no. 10, pp. 2678–2687, 2019.
[45] X. Dai, J.-C. Jiang, and J.-Q. Wu, "Charging area determining and power enhancement method for multiexcitation unit configuration of wirelessly dynamic charging EV system," *IEEE Trans. Ind. Electron.*, vol. 66, no. 5, pp. 4086–4096, May 2019.
[46] Z. Huang, S.-C. Wong, and C. K. Tse, "Design of a single-stage inductive-power-transfer converter for efficient EV battery charging," *IEEE Trans. Veh. Technol.*, vol. 66, no. 7, pp. 5808–5821, Jul. 2017.
[47] K. Onai and J. O. Ojo, "Performance analysis and design of frequency controlled series-series compensated inductive power transfer system for electric vehicle battery charging," *IEEE Trans. Ind. Appl.*, vol. 58, no. 1, pp. 962–973, Jan./Feb. 2022.
[48] S. Lu, T. Lämmle, and N. Parspour, "Analysis and design of a T-compensation network with switch-controlled capacitor for wireless power transfer system," in *Proc. IEEE PELS Workshop Emerg. Technol.: Wireless Power Transfer*, 2021, pp. 1–6.

Shufan Li received the Ph.D. degree in electrical engineering from the Institute of Electrical Engineering, Chinese Academy of Sciences, Beijing, China, in 2020.

He is currently an Assistant Researcher with the Department of Vehicle Energy System and Control Technology, Institute of Electrical Engineering, Chinese Academy of Sciences. His research interests include analysis, designing, and controlling of static/dynamic wireless power transfer system.

Fang Li received the Ph.D. degree in electrical engineering from the Institute of Electrical Engineering, Chinese Academy of Sciences, Beijing, China, in 2009.

She is currently an Associate Professor with the Department of Vehicle Energy System and Control Technology, Institute of Electrical Engineering. Her research interests include wireless power transmission, simultaneous wireless information and power transfer, and intelligent vehicle control.

Rong Zhang received the M.S. degree in electrical engineering from the North China University of Technology, Beijing, China, in 2019.

He is currently an Assistant Researcher with the Department of Vehicle Energy System and Control Technology, Institute of Electrical Engineering, Chinese Academy of Sciences, Beijing, China. His research interests include designing and control of power converters, and optical communication technology.

Lingbing Gong received the M.S. degree in electrical engineering from the Beihang University, Beijing, China, in 2019.

She is currently an Assistant Researcher with the Department of Vehicle Energy System and Control Technology, Institute of Electrical Engineering, Chinese Academy of Sciences, Beijing, China. Her research interests include wireless power transmission and charge control technology.

Chengxuan Tao received the M.S. degree in control science and engineering from the Chongqing University, Chongqing, China, in 2012. He is currently working toward the Ph.D. degree in mechanical engineering with the Beijing Institute of Technology, Beijing, China.

He is currently a Senior Engineer with the Key Laboratory of Power Electronics and Electric Drives, Chinese Academy of Sciences, Beijing, China. His research interests include circuit topology, analysis, and control of wireless power transfer system, especially its applications in special fields.

Lifang Wang (Member, IEEE) received the Ph.D. degree in automotive engineering from Jilin University, Jilin, China, in 1997.

She joined the Institute of Electrical Engineering, Chinese Academy of Sciences (IEECAS), Beijing, China. During the Chinese tenth-five-year plan (2001–2005), she was a member of the national specialist group of the Key Special Electric Vehicle Project of the National 863 Program, and she was the Head of the 863 Special EV Project Office. She is currently the Director of the Department of Vehicle Energy System and Control Technology, IEECAS. She is also the Vice Director of the Key Laboratory of Power Electronics and Electric Drives, Chinese Academy of Sciences. Her research interests include wireless charging system for EV, EV control system, EV battery management system, electromagnetic compatibility, and smart electricity use.